AIAA SciTech Forum
8–12 January 2018, Kissimmee, Florida
2018 AIAA Aerospace Sciences Meeting

10.2514/6.2018-0330

Simulation of 3D Co-Flow Jet Airfoil with Embedded Micro-Compressor Actuator

Yan Ren * Gecheng Zha †
Dept. of Mechanical and Aerospace Engineering
University of Miami, Coral Gables, Florida 33124
E-mail: gzha@miami.edu

Abstract

This paper presents simulations of 3D co-flow jet (CFJ) active flow control airfoil with an embedded micro-compressor actuator. The injection and suction ducts geometries, slot locations and micro-compressor interface boundary conditions are determined based on the design of 2D CFJ airfoil and micro-compressor actuator. The simulations are performed at Mach number 0.15 to simulate the cruise condition of a general aviation aircraft. The airfoil used in this work is CFJ-NACA-6421. The simulations employ 3D RANS solver with Spalart-Allmaras (S-A) turbulence model, 3th order WENO scheme for the inviscid fluxes, and 2nd order central differencing for the viscous terms.

The aerodynamic performance, energy expenditure, and 3D flow field are compared between the CFJ airfoils with different jet momentum coefficient (C_μ) and maximum swirl angle at the injection duct inlet (β_{max}). An CFJ airfoil with ideal ducts and a baseline airfoil are also studied as reference for comparison. The parametric study results show that the lift coefficient (C_L) and power coefficient (P_c) linearly increase with the rise of C_μ, while the drag coefficient (C_D) and productivity efficiency ($(C_L^2/C_D)_c$) linearly decreases with the rise of C_μ. A large β_{max} leads to a more favorable mass flow rate distribution at the injection slot, which suppresses the flow separation at the injection slot edges and improves the aerodynamic performance. However, a too large β_{max} leads to flow separation inside the injection duct and increase the pumping energy loss. The results of this work will guide the future high efficiency CFJ airfoil design optimization and the design for wind tunnel testing with embedded micro-compressors.

Nomenclature

CFJ	Co-flow jet
AoA	Angle of attack
LE	Leading Edge
TE	Trailing Edge
β_{max}	Maximum Injection Duct Inlet Swirl Angle
S	Planform area
s	Wing Span length
c	Profile chord
U	Flow velocity
q	Dynamic pressure $0.5\,\rho U^2$

* Postdoc Researcher, Ph.D., AIAA member
† Professor, ASME Fellow, AIAA associate Fellow

p	Static pressure
ρ	Air density
$\dot{m}$	Mass flow
M	Mach number
ω	Pitching Moment
P	Pumping power
∞	Free stream conditions
j	Jet conditions
C_L	Lift coefficient $L/(q_\infty S)$
C_D	Drag coefficient $D/(q_\infty S)$
C_μ	Jet momentum coef. $\dot{m}_j U_j/(q_\infty S)$
Pc	Power coefficient $L/(q_\infty S V_\infty)$
$(C_L^2/C_D)_c$	CFJ airfoil corrected productivity efficiency $C_L^2/(C_D + P_c)$

1 Introduction

Recently, Co-Flow Jet (CFJ) flow control method developed by Zha et al. [1, 2, 3, 4, 5, 6, 7, 8, 9, 10, 11] is demonstrated to achieve radical lift augmentation, stall margin increase, drag reduction for stationary and pitching airfoils. In the CFJ airfoil concept, an injection slot near the leading edge (LE) and a suction slot near the trailing edge (TE) on the airfoil suction surface are created. As shown in Fig. 1, a small amount of mass flow is withdrawn into the suction duct, pressurized and energized by a micro compressor, and then injected near the LE tangentially to the main flow via a injection duct. The whole process does not add any mass flow to the system and hence is a zero-net mass-flux (ZNMF) flow control. The validity of CFJ flow control method in CFJ-NACA-6421 airfoil has been proved in our previous publication using 3D simulations [8]. However, the micro compressor, injection and suction ducts were idealized for simplicity in that work. The aerodynamic performance of CFJ airfoil in realistic configuration with micro-compressor actuator embedded need to be studied.

In this work, we presents simulations of 3D CFJ active flow control airfoil with an embedded compressor actuator along with suction and injection ducts to simulate realistic flow fields in cruise flight condition. The suction duct is connected to the micro-compressor actuator inlet and the injection duct is connected to the micro-compressor outlet. The duct inlet and outlet size and location are determined by the 2D CFJ airfoil design, so is the associated boundary conditions. The boundary conditions of the micro-compressor is determined by the design of the micro-compressor that meets the CFJ airfoil mass flow and pressure ratio requirements. The injection duct inlet is directly connected to the outlet of the micro-compressor, which presents a ring shape outline and generates swirl flow. In order to remove flow separation, a center-body connecting to the inner circle of the micro compressor outlet is used to guild the flow. Parametric studies are performed to investigate the effect of C_μ and injection duct inlet maximum swirl angle β_{max}. The conclusion of this work could provide guidance for the future high-efficiency CFJ wing design optimization.

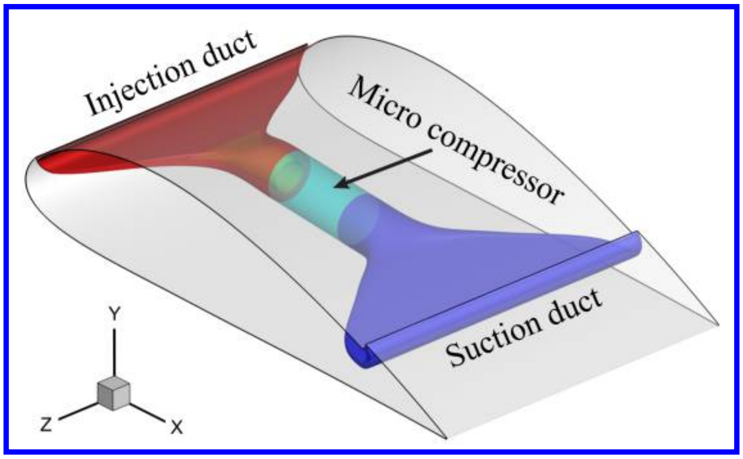

Figure 1: Schematic plot of a typical CFJ airfoil.

2 Methodology

2.1 Lift and Drag Calculation

The momentum and pressure at the injection and suction slots produce a reactionary force, which is automatically measured by the force balance in wind tunnel testing. However, for CFD simulation, the full reactionary force needs to be included. Using control volume analysis, the reactionary force can be calculated using the flow parameters at the injection and suction slot opening surfaces. Zha et al. [2] give the following formulations to calculate the lift and drag due to the jet reactionary force for a CFJ airfoil. By considering the effects of injection and suction jets on the CFJ airfoil, the expressions for these reactionary forces are given as :

$$F_{x_{cfj}} = (\dot{m}_j V_{j1} + p_{j1} A_{j1}) * cos(\theta_1 - \alpha) - (\dot{m}_j V_{j2} + p_{j2} A_{j2}) * cos(\theta_2 + \alpha) \tag{1}$$

$$F_{y_{cfj}} = (\dot{m}_{j1} V_{j1} + p_{j1} A_{j1}) * sin(\theta_1 - \alpha) + (\dot{m}_{j2} V_{j2} + p_{j2} A_{j2}) * sin(\theta_2 + \alpha) \tag{2}$$

where the subscripts 1 and 2 stand for the injection and suction respectively, and θ_1 and θ_2 are the angles between the injection and suction slot's surface and a line normal to the airfoil chord. α is the angle of attack.

The total lift and drag on the airfoil can then be expressed as:

$$D = R'_x - F_{x_{cfj}} \tag{3}$$

$$L = R'_y - F_{y_{cfj}} \tag{4}$$

where R'_x and R'_y are the surface integral of pressure and shear stress in x (drag) and y (lift) direction excluding the internal ducts of injection and suction. For CFJ wing simulations, the total lift and drag are calculated by integrating Eqs.(3) and (4) in the spanwise direction.

2.2 Jet Momentum Coefficient

The jet momentum coefficient C_μ is a parameter used to quantify the jet intensity. It is defined as:

$$C_\mu = \frac{\dot{m}V_j}{\frac{1}{2}\rho_\infty {V_\infty}^2 S} \tag{5}$$

where $\dot{m}$ is the injection mass flow, V_j is the mass-averaged injection velocity, ρ_∞ and V_∞ denote the free stream density and velocity, and S is the planform area.

2.3 Power Coefficient

CFJ is implemented by mounting a pumping system inside the wing that withdraws air from the suction slot and blows it into the injection slot. The power consumption is determined by the jet mass flow and total enthalpy change as the following:

$$P = \dot{m}(H_{t1} - H_{t2}) \tag{6}$$

where H_{t1} and H_{t2} are the mass-averaged total enthalpy in the injection cavity and suction cavity respectively, P is the Power required by the pump and $\dot{m}$ the jet mass flow rate. Introducing P_{t1} and P_{t2} the mass-averaged total pressure in the injection and suction cavity respectively, the pump efficiency η, and the total pressure ratio of the pump $\Gamma = \frac{P_{t1}}{P_{t2}}$, the power consumption is expressed as:

$$P = \frac{\dot{m}C_p T_{t2}}{\eta}(\Gamma^{\frac{\gamma-1}{\gamma}} - 1) \tag{7}$$

where γ is the specific heat ratio equal to 1.4 for air. The power coefficient is expressed as:

$$P_c = \frac{P}{\frac{1}{2}\rho_\infty V_\infty^3 S} \tag{8}$$

2.4 Corrected Productivity Efficiency

The conventional wing productivity efficiency is defined as:

$$\frac{C_L^2}{C_D} \tag{9}$$

For the CFJ wing, the ratio above still represents the pure aerodynamic relationship between lift coefficient and drag coefficient. However since CFJ active flow control consumes energy, the ratio above is modified to take into account the energy consumption of the pump. The formulation of the corrected productivity efficiency for CFJ wings is:

$$(\frac{C_L^2}{C_D})_c = \frac{C_L^2}{C_D + P_c} \tag{10}$$

where P_c is the pumping power coefficient defined in Eqn. 8 and C_L and C_D are the lift and drag coefficients of the CFJ wing. If the pumping power coefficient is set to 0, this formulation returns to the productivity efficiency of a conventional wing.

2.5 CFD Simulation Setup

The FASIP (Flow-Acoustics-Structure Interaction Package) CFD code is used to conduct the numerical simulation. The 3D Reynolds Averaged Navier-Stokes (RANS) equations with one-equation Spalart-Allmaras [12] turbulence model is used. A 3rd order WENO scheme for the inviscid flux [13, 14, 15, 16, 17, 18] and a 2nd order central differencing for the viscous terms [13, 17] are employed to discretize the Navier-Stokes equations. The low diffusion E-CUSP scheme used as the approximate Riemann solver suggested by Zha et al [14] is utilized with the WENO scheme to evaluate the inviscid fluxes. Implicit time marching method using Gauss-Seidel line relaxation is used to achieve a fast convergence rate [19]. Parallel computing is implemented to save wall clock simulation time [20].

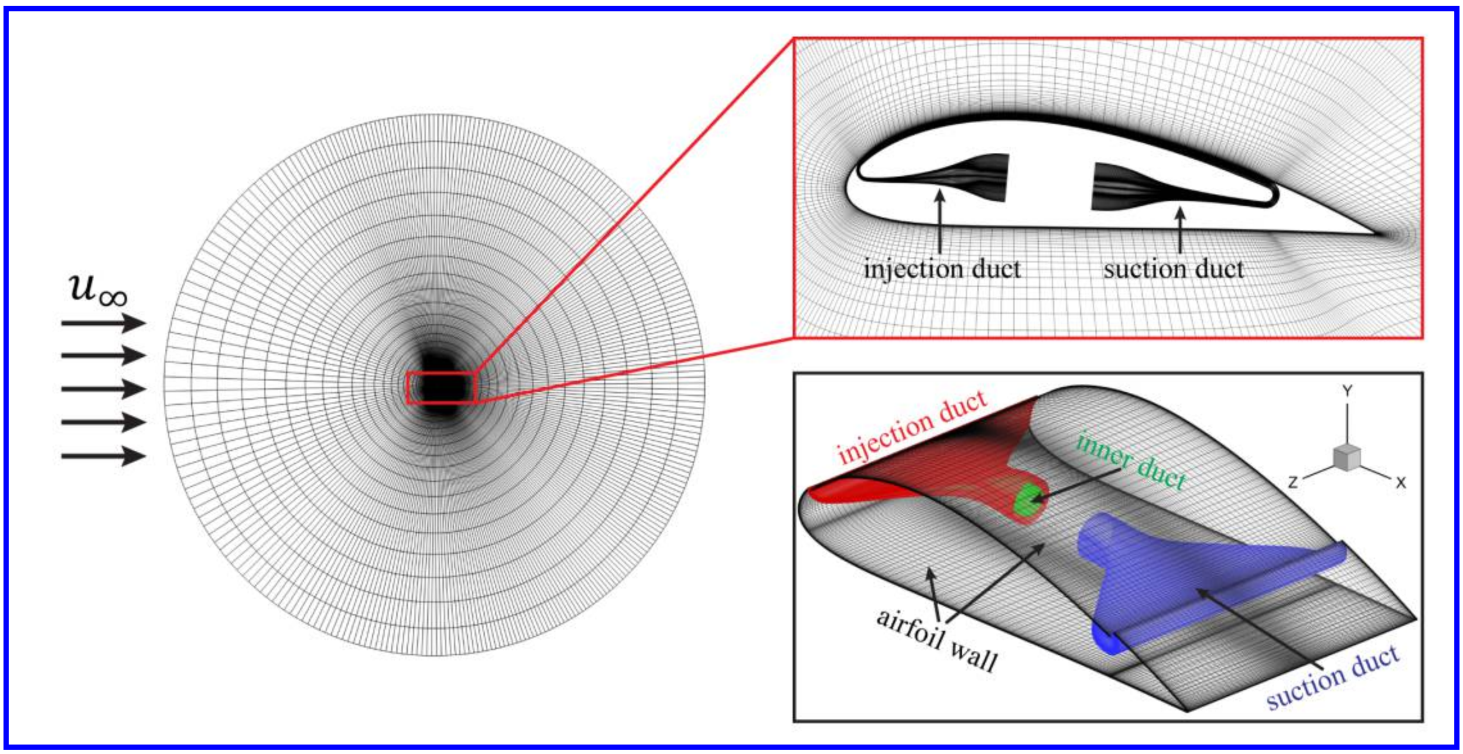

Figure 2: Computational mesh used in the current work.

2.6 Boundary Conditions

The 3rd order accuracy no slip condition is enforced on the solid surface with the wall treatment suggested in [21] to achieve the flux conservation on the wall. The computational mesh is shown in Fig. 2. Total pressure, total temperature and flow angles are specified at the injection duct inlet, as well as the upstream portion of the far field. Constant static pressure is applied at the suction duct outlet as well as the downstream portion of the far field. The micro-compressor inlet and outlet profiles[22] are used as the boundary conditions of the suction duct outlet and injection inlet to simulate the micro-compressor actuator effects. Symmetry boundary conditions are applied at the two sides in z-direction to ensure the effect of a segment of a 3D CFJ wing. The cross-section faces of the ducts are meshed using "H" topology while the parts around the airfoil are meshed using "O" topology. The total mesh size is 11.376 millions points, split into 192 blocks for the parallel computation. The first grid point on the wing surface is placed at $y^+ \approx 1$.

3 Results and Discussion

The parametric study results are presented in this section. The effect of C_μ and β_{max} are discussed in detail. A case with ideal injection and suction ducts (case ID) and a baseline case without CFJ flow control (case BL) will also be studied. The corresponding case parameters are listed in Table 1.

Table 1: Simulation parameters used in the current work.

Cases	C_μ	β_{max}	Mach	AoA	Airfoil
C1	0.04	64.04°	0.15	5°	CFJ-NACA-6421
C2	0.06	64.04°	0.15	5°	CFJ-NACA-6421
C3	0.08	64.04°	0.15	5°	CFJ-NACA-6421
C4	0.10	64.04°	0.15	5°	CFJ-NACA-6421
C5	0.12	64.04°	0.15	5°	CFJ-NACA-6421
C6	0.04	25.62°	0.15	5°	CFJ-NACA-6421
C7	0.04	38.42°	0.15	5°	CFJ-NACA-6421
C8	0.04	51.23°	0.15	5°	CFJ-NACA-6421
C9	0.04	76.85°	0.15	5°	CFJ-NACA-6421
ID	0.04	0°	0.15	5°	CFJ-NACA-6421
BL	N/A	N/A	0.15	5°	NACA6421

3.1 The Effect of Jet Momentum Coefficient, C_μ

In this section, the effect of jet momentum coefficient (C_μ) on the CFJ airfoil performance is investigated. Five cases (C1 - C5) are studied with the C_μ varying from 0.04 to 0.12. The corresponding results are shown in Fig. 3. We can see from Fig. 3 (a) that C_L is almost linearly increased with the rise of C_μ. In contrast, C_D is decreased. The cases with large C_μ (case C4 and C5) obtain negative drag (thrust). This suggests that more flow control capacity is obtained with stronger jet, and hence better aerodynamic performance is achieved with higher C_μ. In the other hand, as shown in Fig. 3 (b), the P_c linearly increases with the rise of C_μ. More energy is consumed to sustain a greater jet. This leads to the decrease of the productivity efficiency in terms of $(C_L^2/C_D)_c$.

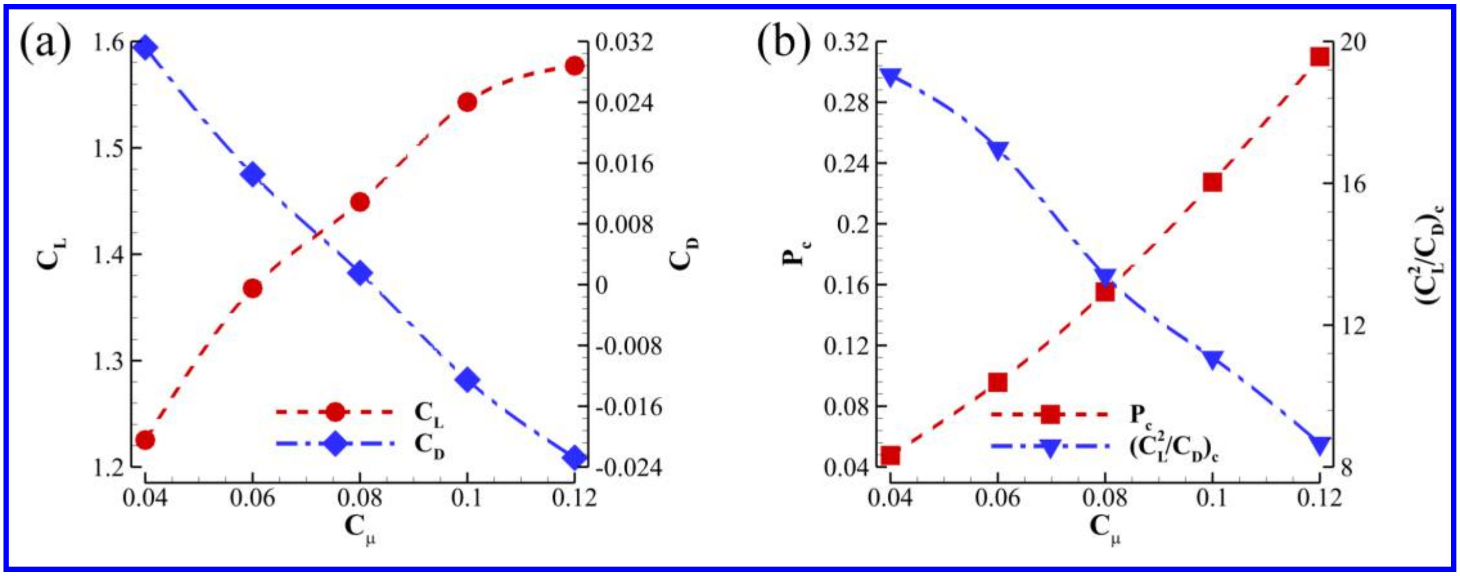

Figure 3: Aerodynamic performance of the cases with different C_μ, (a) C_L and C_D; (b) P_c and $(C_L^2/C_D)_c$.

The effect of C_μ on the flow field is described in the following. Two cases with C_μ of 0.04 and 0.12 (C1 and C5) are chosen for comparison according to Fig. 3 since they represent the most differences in C_μ and aerodynamic performance. The 2D flow slices at the the mid span of the two cases are compared first. As shown in Fig. 4, both cases show well attached flow at the mid span, while the case C5 shows much greater Mach number within the injection and suction ducts. Also, much stronger jet near the suction surface of the airfoil can be observed for case C5. It leads to the drop of the static pressure at the suction side of the airfoil and hence improve the C_L for case C5.

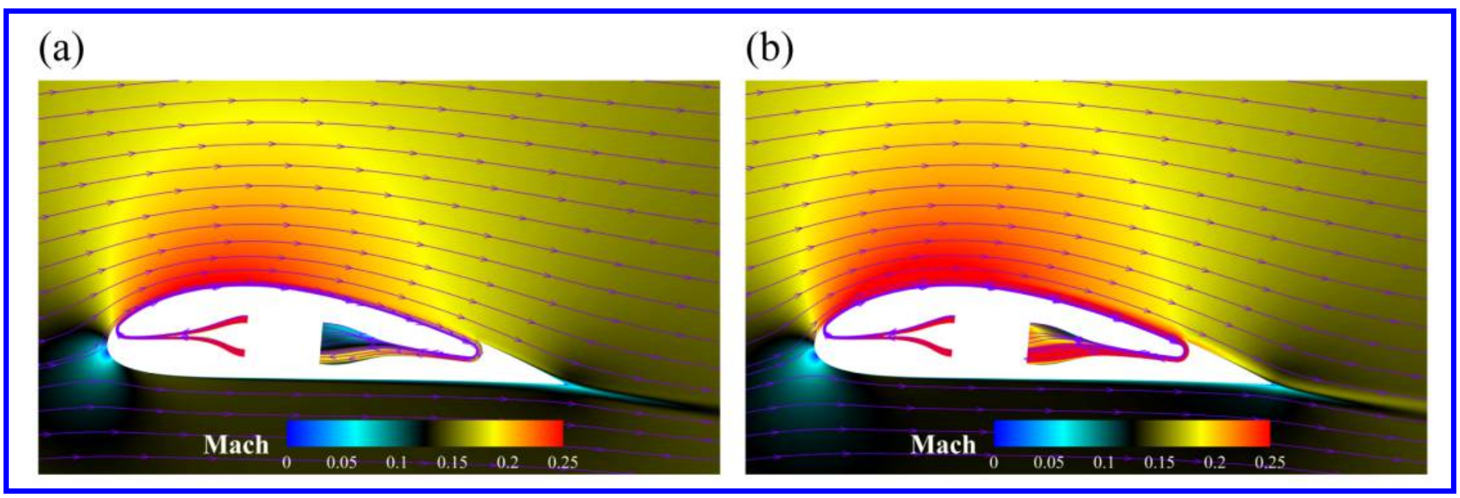

Figure 4: 2D flow slices at the mid span, (a) case C1; (b) case C5.

Next, we look at the 3D streamlines around the wing segments for the two cases. As shown in Fig. 5 (a) and (c), for both cases, most parts of the wings have attached flow, except for small regions near the edges of the injection slot with flow separation. We further look at the flow slices at the airfoil edges. As shown in Fig. 5 (b) and (d), the flow separation for case C5 is much smaller. It leads to the drop of C_D for case C5. Even though the case C5 shows much greater lift and much less drag, the productivity efficiency in terms of $(C_L^2/C_D)_c$ decreases a lot due to the large power coefficient P_c needed for the micro-compressor to provide the stronger jet in case C5.

The flow separation at the edges of the CFJ wings is due to the unevenly distributed mass flow rate in span wise direction at the injection slot. Since the injection duct inlet is directly connected to the outlet of the micro-compressor with swirl flow, the swirl could be used to push the flow to the two edges of the wing near the injection slot. Next, we will discuss the effect of the swirl flow at the injection duct inlet.

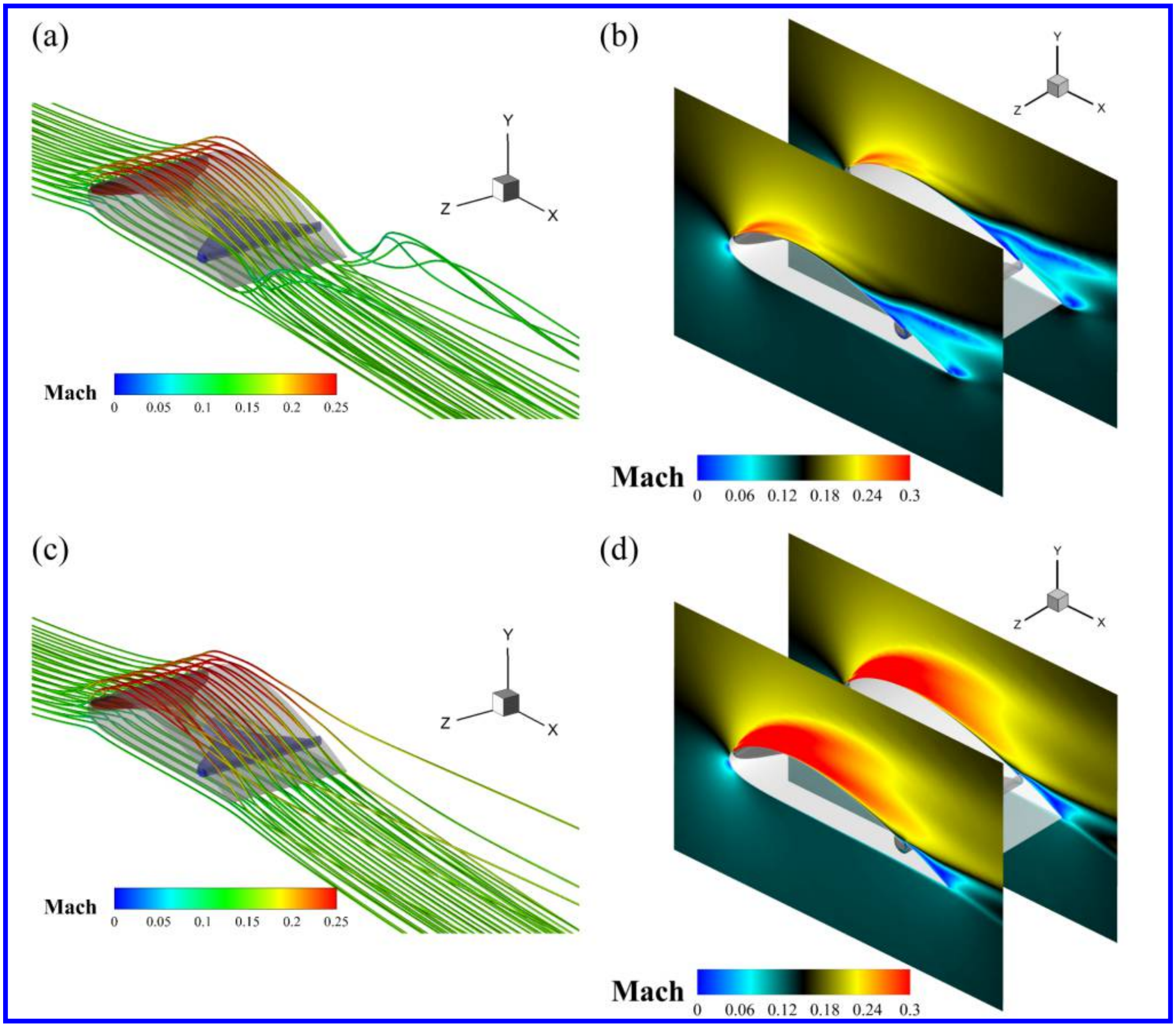

Figure 5: 3D streamlines near the airfoil and 2D flow slices at the airfoil edges, (a) (b) case C1; (c) (d) case C5.

3.2 The Effect of Swirl Flow at Injection Duct Inlet

In this sub-section, the effect of maximum swirl angle at the injection duct inlet (β_{max}) on the CFJ airfoil performance is investigated. Five cases (C6, C7, C8, C1, C9) are studied, with the β_{max} varies from 25.62° to 76.85°. Fig. 6 shows the swirl angle radial profile at the injection duct inlet for the five cases. The corresponding results are shown in Fig. 7. Two distinct regions of β_{max} with different trends of the aerodynamic performance can be identified in Fig. 7. The first region is from $\beta_{max} \approx 25°$ to $\beta_{max} \approx 50°$. In this region, when the β_{max} increases, the C_L increases, the C_D decreases, the P_c stays unchanged, and the $(C_L^2/C_D)_c$ also increases. The second region locates from $\beta_{max} \approx 50°$ to $\beta_{max} \approx 80°$. In this region, when the β_{max} increases, the C_L decreases, the C_D increases, the P_c also increases, and the $(C_L^2/C_D)_c$ decrease.

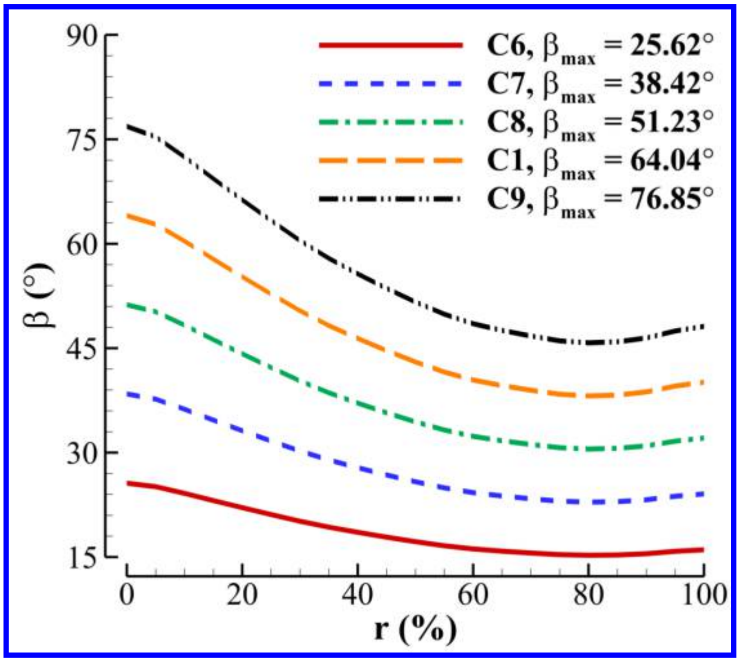

Figure 6: Aerodynamic performance of the cases with different β_{max}, (a) C_L and C_D; (b) P_c and $(C_L^2/C_D)_c$.

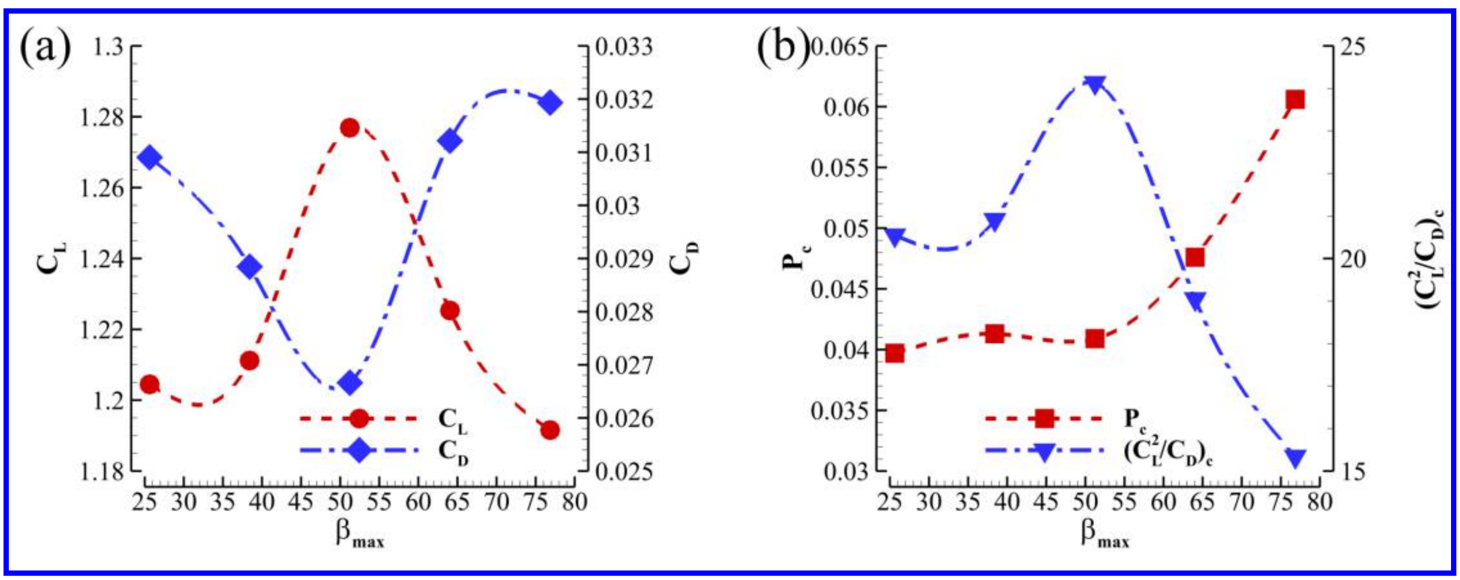

Figure 7: Radial profiles of the swirl angle for the case C6, C7, C8, C1, and C9.

Next, the flow fields of three typical cases (case C6, C8, and C9) with β_{max} of 25.62°, 51.23°, 76.85° respectively are investigated in detail. Fig. 8 shows the 2D flow slices at the mid span of the three cases. We can see that all cases show similar flow patterns and present well attached flow at the mid span. Fig. 9 (a), (c), and (e) show the

3D stream lines near the airfoil surfaces of the three cases. Similar to case C1 and C5 in the previous sub-section, all the three cases show flow separation at the injection slot edges. Other parts of the wing show well attached flow for the three cases. We further look at the 2D flow slices at the injection slot edges for the three cases. The results are plotted in Fig. 9 (b), (d), and (f). We can see that the flow separation for case C6 and C9 show similar pattern, while that for case C8 is a bit smaller.

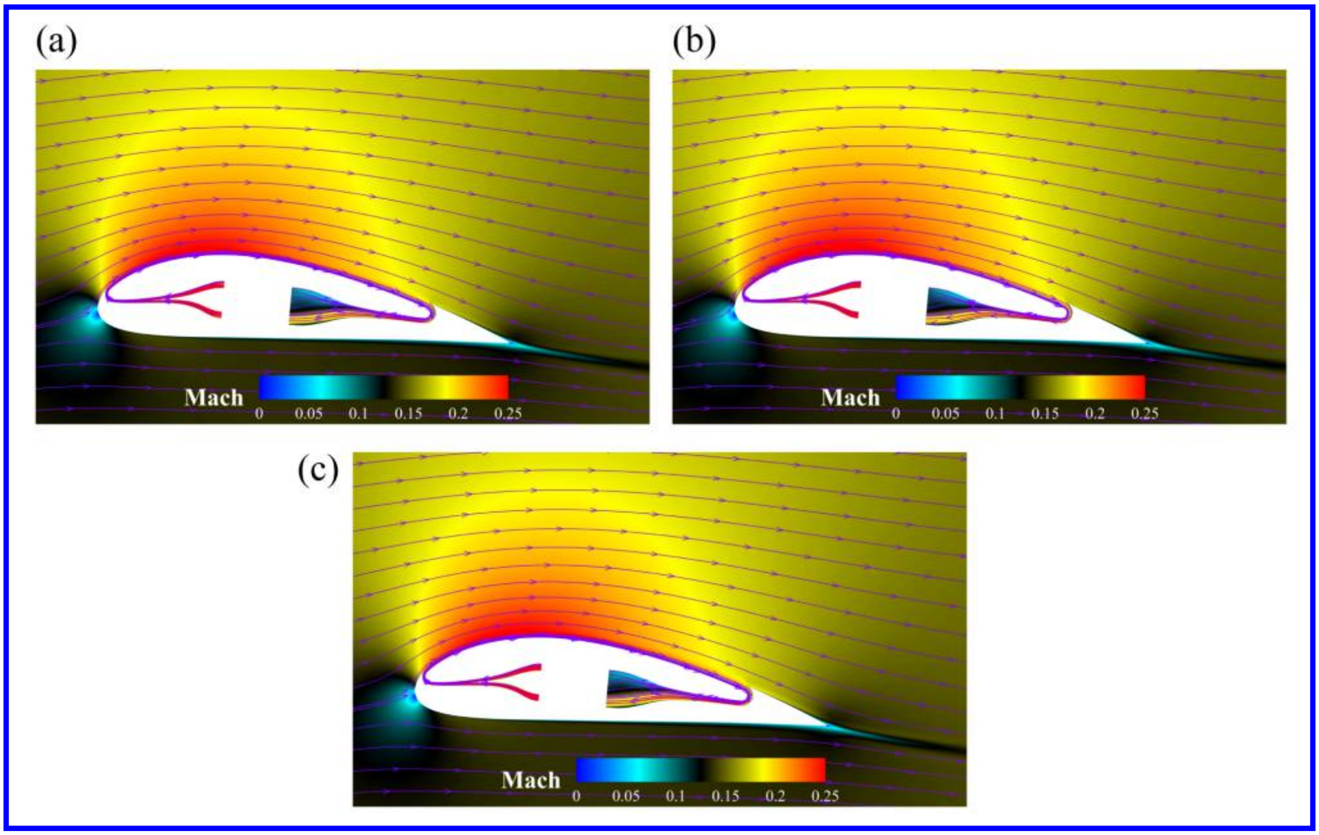

Figure 8: 2D flow slices at the mid span, (a) case C6; (b) case C8; (c) case C9.

For case C6 and C8, the Mach contours at the injection slot are plotted in Fig. 10 (a) and (b). To more clearly view the flow field, the plot is not in the actual aspect ratio. The vertical dimension is enlarged by 312 times. We can see that the case C8 shows two zones with a little higher velocity near the two injection slot edges ($span \approx \pm 0.26$). It suggests that the case C8, which has greater swirl angle at the injection duct inlet, has more flow at the injection slot edges. We further plot the mass flow rate distributions at the injection slot in span wise direction for the two cases in Fig. 10 (d). The results show that the mass flow rate at the two edges for the case C8 is 10.4% greater than that of the case C6. We can conclude that a greater β_{max} leads to a more favorable mass flow rate distribution at the injection slot, which suppresses the flow separation at the injection slot edges and improves the aerodynamic performance. That explains the trends in the first region ($25^\circ \leq \beta_{max} \leq 50^\circ$) of β_{max} (Fig. 7).

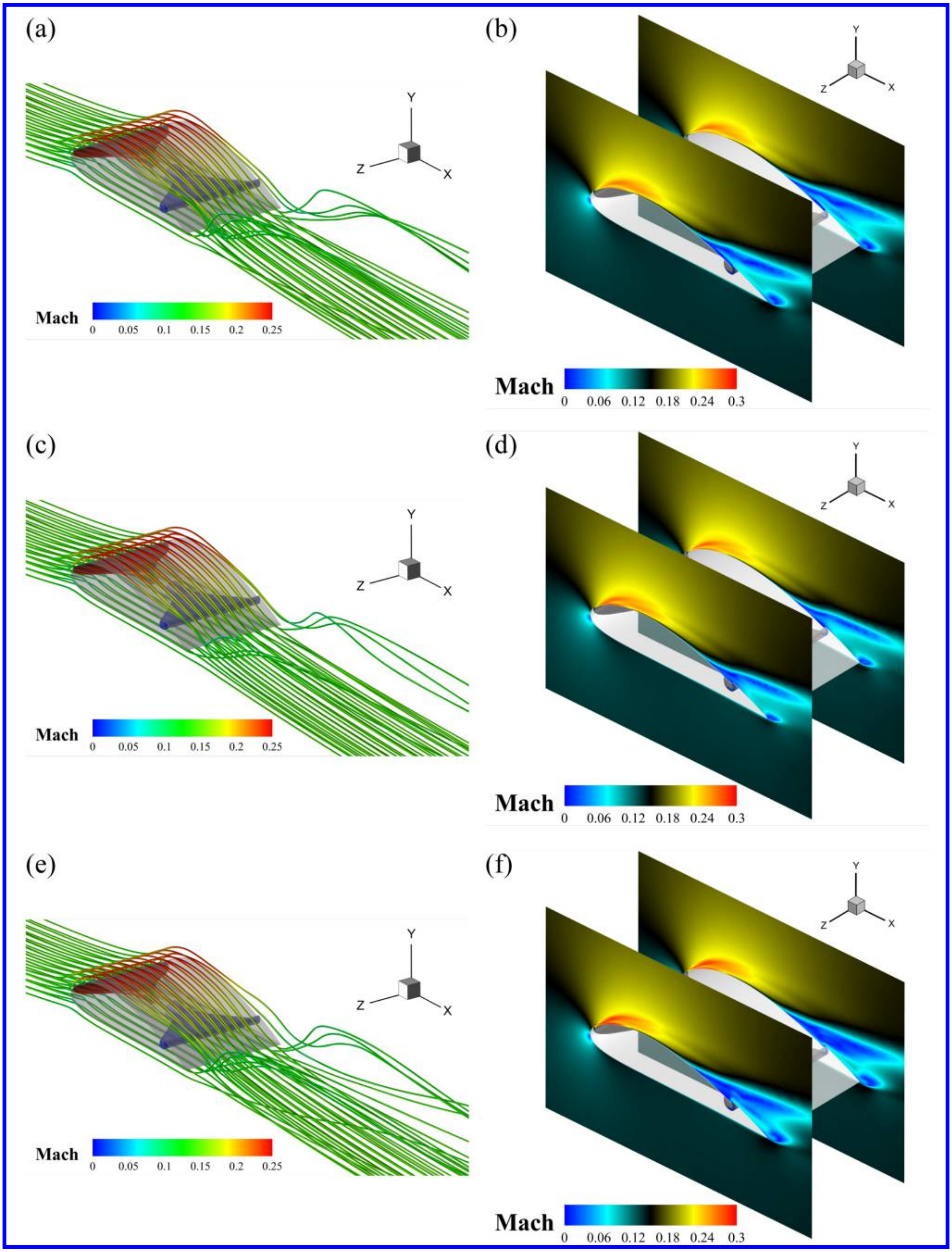

Figure 9: 3D streamlines near the airfoil and 2D flow slices at the airfoil edges, (a) (b) case C6; (c) (d) case C8; (e) (f) case C9.

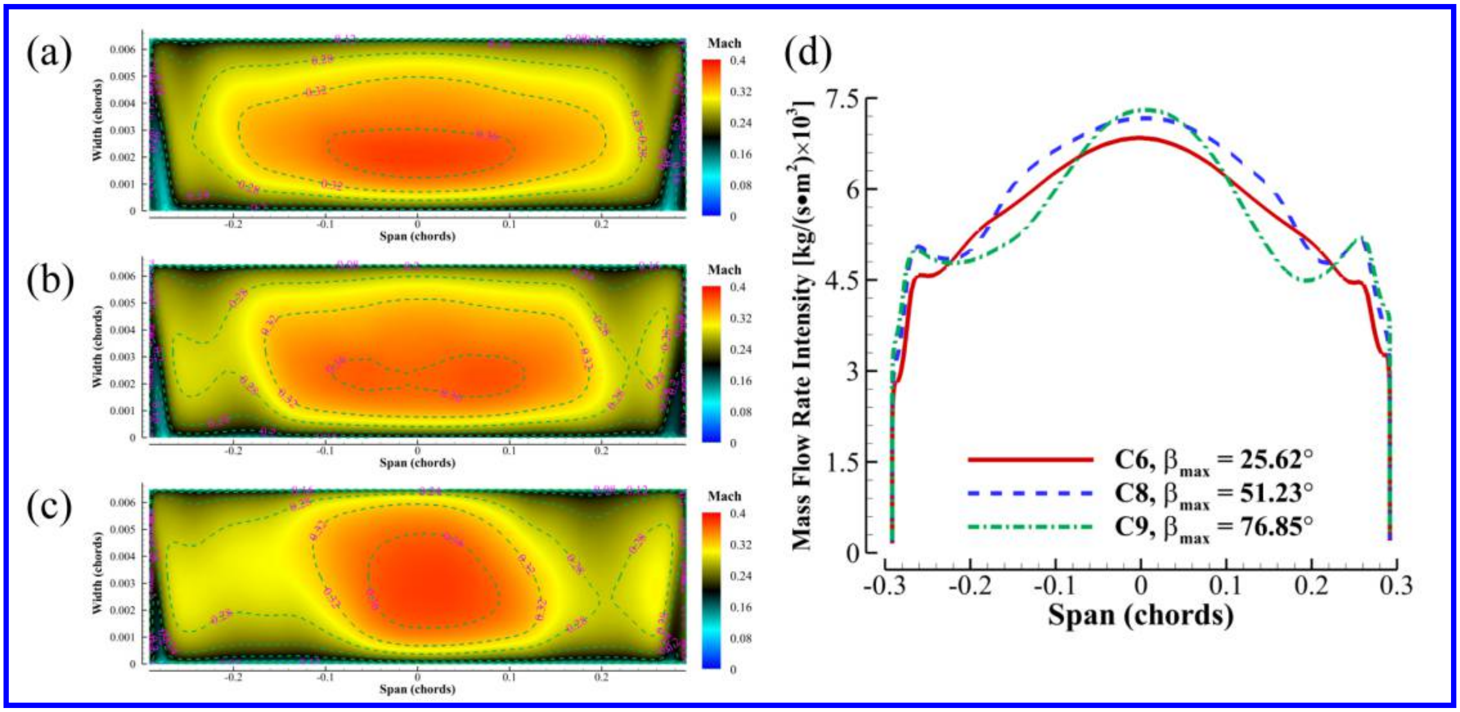

Figure 10: Mach contours at the injection slot for (a) case C6, (b) case C8, and (c) case C9; (d) mass flow rate distribution in span wise direction at the injection slot of case C6, C8, and C9.

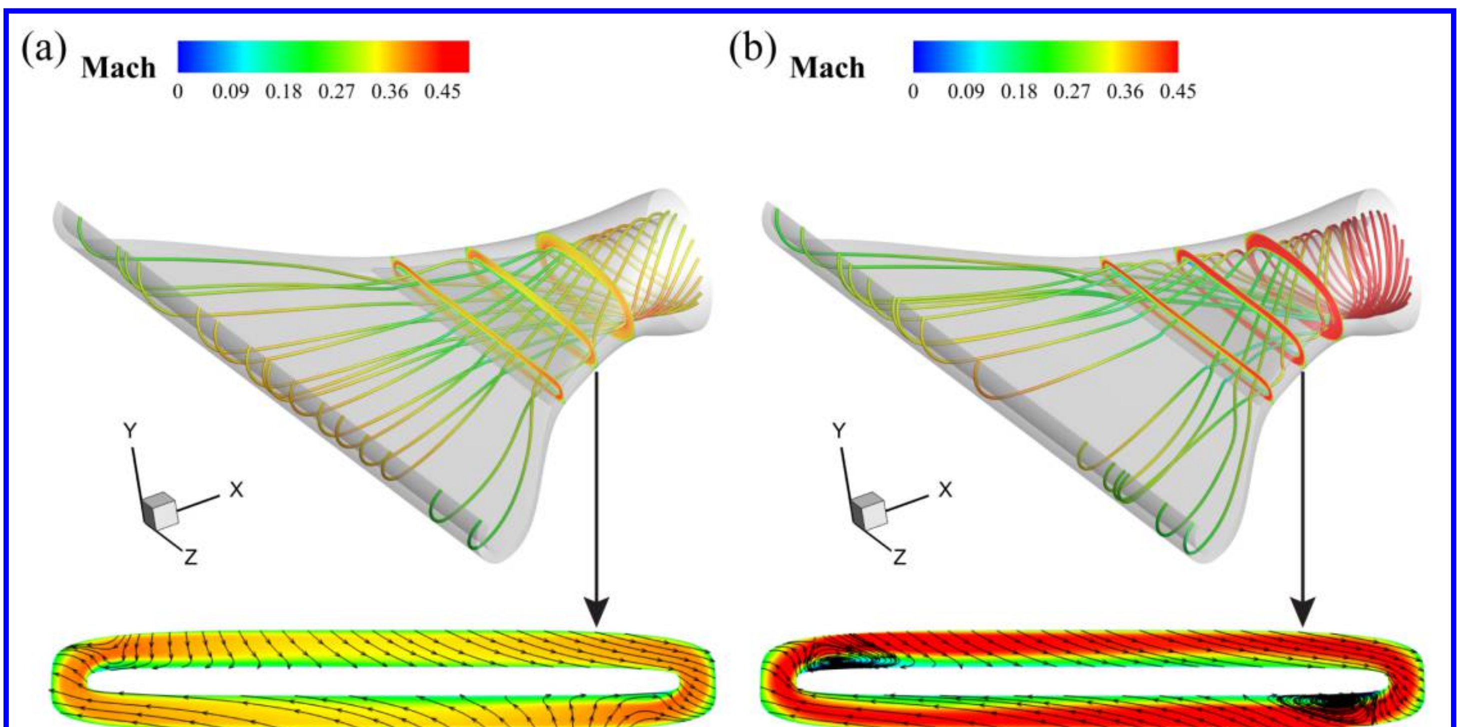

Figure 11: 3D streamlines and 2D flow slices along the stream wise direction of the injection duct of (a) case C8 and (b) case C9.

For case C6 and C8, the Mach contours at the injection slot are plotted in Fig. 10 (a) and (b). To more clearly view the flow field, the plot is not in the actual aspect ratio. The vertical dimension is enlarged by 312 times. We can see that the case C8 shows two zones with a little higher velocity near the two injection slot edges ($span \approx \pm 0.26$). It suggests that the case C8, which has greater swirl angle at the injection duct inlet, has more flow at the injection slot edges. We further plot the mass flow rate distributions at the injection slot in span wise direction for the two cases in Fig. 10 (d). The results show that the mass flow rate at the two edges for the case C8 is 10.4% greater than that of the case C6. We can conclude that a greater β_{max} leads to a more favorable mass flow rate distribution at the injection slot, which suppresses the flow separation at the injection slot edges and improves the aerodynamic performance. That explains the trends in the first region ($25^\circ \leq \beta_{max} \leq 50^\circ$) of β_{max} (Fig. 7).

To see the effect of increasing β_{max} from 51.23° for Case 8 to 76.85° for Case 9, 3D streamlines inside the injection ducts are plotted in Fig. 11. We further cut flow slices along the stream wise direction and plot 2D streamlines on the slices. We can see that the case C9 shows flow separation near the corner of the injection duct, which creates flow blockage and decreases the mass flow rate (Fig. 10 c and d). The flow separation also increase the energy loss and degrade the overall performance of the CFJ airfoil. We can conclude that too large β_{max} leads to flow separation inside the injection duct and increase the energy loss. This explains the trends in the second region ($50^\circ \leq \beta_{max} \leq 80^\circ$) of β_{max} (Fig. 7).

In summary, the optimum β_{max} is around 50°, which is large enough to provide a favorable mass flow distribution at the injection slot and is small enough to prevent the flow separation inside the injection duct.

3.3 CFJ Airfoil with Ideal Ducts

In this sub-section, the aerodynamic performance of CFJ airfoil with ideal (ID) injection and suction ducts are studied. Three cases defined in Table 1 are selected for comparison: a) the ideal (ID) CFJ airfoil case with uniform injection and suction slot flow at C_μ of 0.04; b) the baseline (BL) case with no CFJ; c) Case C8 with the same C_μ as that for ID case, but with the maximum swirl angle of $\beta_{max} = 51.23^\circ$. The purpose of this comparison is two folds: 1) to see the advantages of the CFJ flow control under ideal uniform injection and suction(case ID) over the baseline airfoil with no flow control; 2) to compare the performance loss between the uniform injection and suction(case ID) with the jet provided by a micro-compressor(case C8). Fig. 12 (a) shows a schematic plot of CFJ airfoil with ideal ducts. The ideal ducts are uniform in span wise direction. Boundary conditions are uniformly enforced at all span locations of the injection duct inlet (fixed total pressure and flow angle) and suction duct outlet (fixed static pressure). The loss due to the ducts is minimized in the case ID.

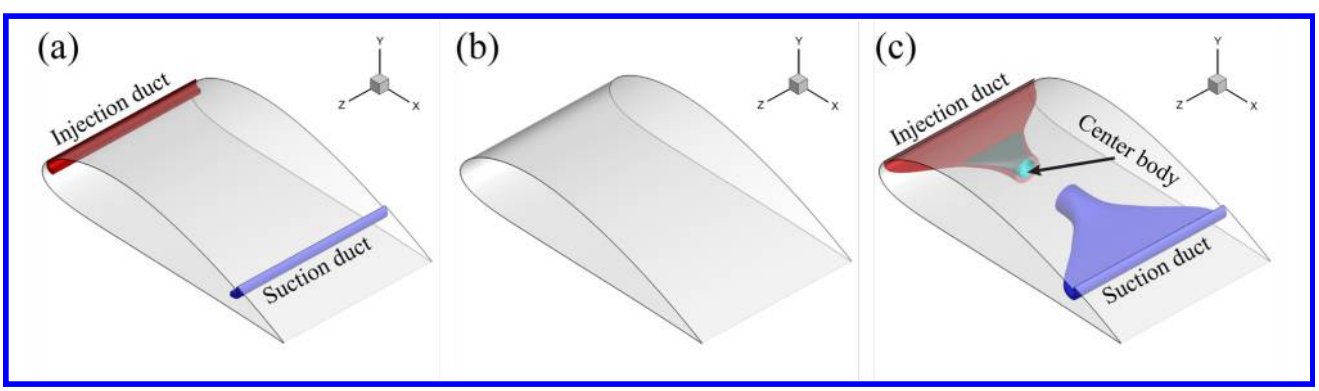

Figure 12: Schematic plots of CFJ-NACA-6421 airfoil, injection duct, and suction duct geometries for (a) case ID, (b) case BL, and (c) case C1.

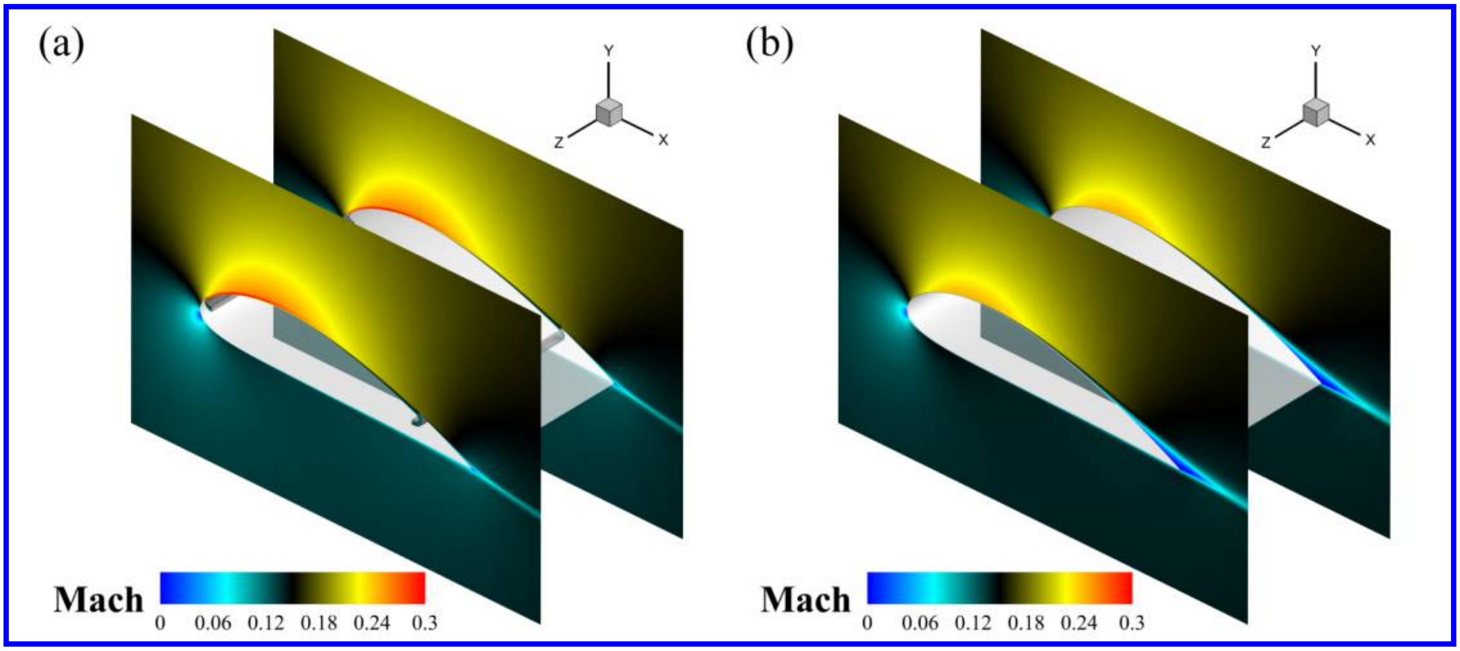

Figure 13: 2D flow slices at the airfoil edges for (a) case ID and (b) case BL.

Table 2: Aerodynamic performance of the three cases.

Cases	C_L	C_D	P_c	$(C_L^2/C_D)_c$
ID	1.39	0.0079	0.0162	79.92
BL	1.01	0.02	N/A	51.04
C8	1.28	0.0267	0.0409	24.13

Fig. 13 shows the flow slices at the edges of the airfoils for case ID and BL. We can see very well attached flow for the case ID, while small flow separation can be observed at the trailing edge of the airfoil for the case BL. Comparing to case C8 (Fig. 9 d), the case ID shows no flow separation across the span including at the slot edges edges. Table 2 lists the aerodynamic performance of the three cases. We can see from the table that the case ID presents much better aerodynamic lift, efficiency, and productivity efficiency than the case BL. The C_L increases by 37.6% and C_D decreases by 65.5%. The $(C_L^2/C_D)_c$ also increases by 56.6%. The case C8 shows an increase of the lift coefficient by 21.8% while the C_D and $(C_L^2/C_D)_c$ suffers substantial loss compared with case ID due to the flow separation at the edges of the injection slot. Fig. 14 shows the mass flow rate distribution at the injection slot in span wise direction for the case ID and C8. We can see from the plot that the ideal case shows a completely flat distribution (no separation) while the case C8 shows a non-uniform distribution (separation at the edges). Thus the direction to optimize the CFJ airfoil efficiency is to provide the uniform jet mass flow distribution at the injection slot.

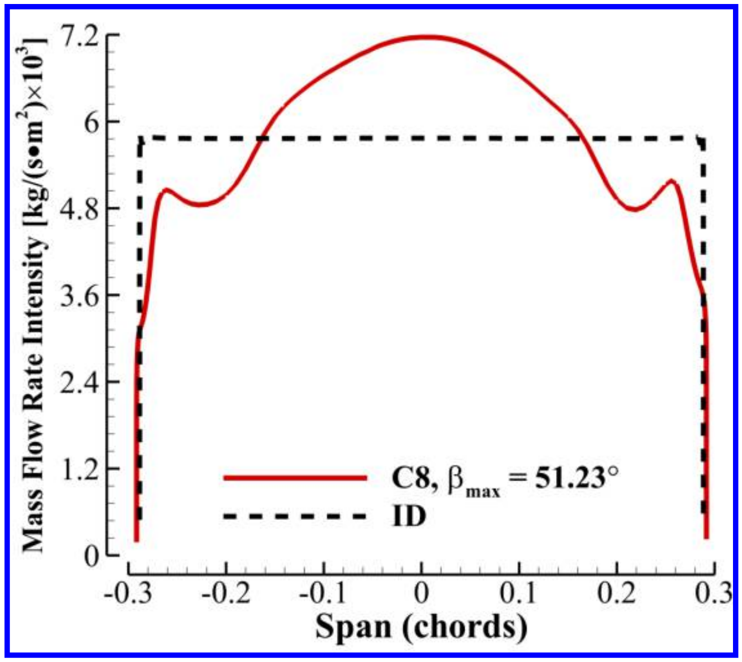

Figure 14: Mass flow rate distribution in span wise direction at the injection slot of case C8 and ID.

4 Conclusion

In this paper, parametric studies are performed to investigate the effect of jet momentum coefficient (C_μ) and maximum swirl angle at injection duct inlet (β_{max}) of CFJ airfoils in cruise flight condition. For the C_μ, we conclude that the C_L and P_c linearly increase with the rise of C_μ, while the C_D and $(C_L^2/C_D)_c$ linearly decreases with the rise of C_μ. larger C_μ corresponds to more flow control capacity to achieve larger C_L and smaller C_D. Also, it consumes more energy to sustain a strong jet, which leads to the increase of the P_c and decrease of the $(C_L^2/C_D)_c$.

For the β_{max}, we conclude that a greater β_{max} leads to a more favorable mass flow rate distribution at the injection slot, which suppresses the flow separation at the airfoil edges and improves the aerodynamic performance. Also, too large β_{max} leads to flow separation inside the injection duct and increase the energy loss. The optimum β_{max} is around 50°, which is large enough to provide a favorable mass flow distribution at the injection slot and is small enough to prevent the flow separation inside the injection duct.

The study of the ideal duct case shows great potential of CFJ flow control airfoil. The C_L increases by 37.6%, the C_D decreases by 65.5%, the $(C_L^2/C_D)_c$ also increases by 56.6% comparing to the airfoil without CFJ flow control. The ideal case also provide guidance to the future highly efficient CFJ airfoil design.

5 Acknowledgment

This project is sponsored by the Defense Advanced Research Projects Agency and monitored by the program manager Jean-Charles Ledé under Cooperative Agreement No.: HR0011-16-2-0052. The content of the information does not necessarily reflect the position or the policy of the Government, and no official endorsement should be

inferred. The simulations are conducted on Pegasus supercomputing system at the Center for Computational Sciences at the University of Miami.

References

[1] G.-C. Zha and D. C. Paxton, “A Novel Flow Control Method for Airfoil Performance Enhancement Using Co-Flow Jet.” *Applications of Circulation Control Technologies*, Chapter 10, p. 293-314, Vol. 214, Progress in Astronautics and Aeronautics, AIAA Book Series, Editors: Joslin, R. D. and Jones, G.S., 2006.

[2] G.-C. Zha, W. Gao, and C. Paxton, “Jet Effects on Co-Flow Jet Airfoil Performance,” *AIAA Journal, No. 6,*, vol. 45, pp. 1222–1231, 2007.

[3] G.-C. Zha, C. Paxton, A. Conley, A. Wells, and B. Carroll, “Effect of Injection Slot Size on High Performance Co-Flow Jet Airfoil,” *AIAA Journal of Aircraft*, vol. 43, 2006.

[4] G.-C. Zha, B. Carroll, C. Paxton, A. Conley, and A. Wells, “High Performance Airfoil with Co-Flow Jet Flow Control,” *AIAA Journal*, vol. 45, 2007.

[5] Wang, B.-Y. and Haddoukessouni, B. and Levy, J. and Zha, G.-C., “Numerical Investigations of Injection Slot Size Effect on the Performance of Co-Flow Jet Airfoil,” *Journal of Aircraft*, vol. Vol. 45, No. 6,, pp. pp.2084–2091, 2008.

[6] B. P. E. Dano, D. Kirk, and G.-C. Zha, “Experimental Investigation of Jet Mixing Mechanism of Co- Flow Jet Airfoil.” AIAA-2010-4421, 5th AIAA Flow Control Conference, Chicago, IL, 28 Jun - 1 Jul 2010.

[7] B. P. E. Dano, G.-C. Zha, and M. Castillo, “Experimental Study of Co-Flow Jet Airfoil Performance Enhancement Using Micro Discreet Jets.” AIAA Paper 2011-0941, 49th AIAA Aerospace Sciences Meeting, Orlando, FL, 4-7 January 2011.

[8] A. Lefebvre, B. Dano, W. Bartow, M. Fronzo, and G. Zha, “Performance and energy expenditure of coflow jet airfoil with variation of mach number,” *Journal of Aircraft*, vol. 53, no. 6, pp. 1757–1767, 2016.

[9] A. Lefebvre, G-C. Zha, “Numerical Simulation of Pitching Airfoil Performance Enhancement Using Co-Flow Jet Flow Control,” *AIAA paper 2013-2517*, June 2013.

[10] A. Lefebvre, G-C. Zha, “Cow-Flow Jet Airfoil Trade Study Part I : Energy Consumption and Aerodynamic Performance,” *32nd AIAA Applied Aerodynamics Conference, AIAA AVIATION Forum, AIAA 2014-2682*, June 2014.

[11] A. Lefebvre, G-C. Zha, “Cow-Flow Jet Airfoil Trade Study Part II : Moment and Drag,” *32nd AIAA Applied Aerodynamics Conference, AIAA AVIATION Forum, AIAA 2014-2683*, June 2014.

[12] P. R. Spalart and S. R. Allmaras, “A one-equation turbulence model for aerodynamic flows,” in *30th Aerospace Sciences Meeting and Exhibit, Aerospace Sciences Meetings, Reno, NV, USA, AIAA Paper 92-0439*, 1992.

[13] Y.-Q. Shen and G.-C. Zha, “Large Eddy Simulation Using a New Set of Sixth Order Schemes for Compressible Viscous Terms ,” *Journal of Computational Physics*, vol. 229, pp. 8296–8312, 2010.

[14] Zha, G.C., Shen, Y.Q. and Wang, B.Y., “An improved low diffusion E-CUSP upwind scheme ,” *Journal of Computer and Fluids*, vol. 48, pp. 214–220, Sep. 2011.

[15] Y.-Q. Shen and G.-Z. Zha , "Generalized finite compact difference scheme for shock/complex flowfield interaction," *Journal of Computational Physics*, vol. doi:10.1016/j.jcp.2011.01.039, 2011.

[16] Shen, Y.-Q. and Zha, G.-C. and Wang, B.-Y., " Improvement of Stability and Accuracy of Implicit WENO Scheme," *AIAA Journal*, vol. 47, No. 2, pp. 331–344, 2009.

[17] Shen, Y.-Q. and Zha, G.-C. and Chen, X.-Y., " High Order Conservative Differencing for Viscous Terms and the Application to Vortex-Induced Vibration Flows," *Journal of Computational Physics*, vol. 228(2), pp. 8283–8300, 2009.

[18] Shen, Y.-Q. and Zha, G.-C. , " Improvement of the WENO Scheme Smoothness Estimator," *International Journal for Numerical Methods in Fluids*, vol. DOI:10.1002/fld.2186, 2009.

[19] G.-C. Zha and E. Bilgen, "Numerical Study of Three-Dimensional Transonic Flows Using Unfactored Upwind-Relaxation Sweeping Algorithm," *Journal of Computational Physics*, vol. 125, pp. 425–433, 1996.

[20] B.-Y. Wang and G.-C. Zha, "A General Sub-Domain Boundary Mapping Procedure For Structured Grid CFD Parallel Computation," *AIAA Journal of Aerospace Computing, Information, and Communication*, vol. 5, No.11, pp. 2084–2091, 2008.

[21] Y.-Q. Shen, G.-C. Zha, and B.-Y. Wang, "Improvement of Stability and Accuracy of Implicit WENO Scheme ," *AIAA Journal*, vol. 47, pp. 331–344, 2009.

[22] PCA engineers, "Design of a mixed flow fan." Internal Report to University of Miami, 2017.